MNRAS 000, 1–12 (2016) Preprint 28 June 2016 Compiled using MNRAS LATEX style file v3.0

The extended disc and halo of the Andromeda galaxy observed with *Spitzer*-IRAC

Masoud Rafiei Ravandi,[1]* Pauline Barmby,[1,2]† Matthew L. N. Ashby,[3] Seppo Laine,[4] T. J. Davidge,[5] Jenna Zhang,[3] Luciana Bianchi,[6] Arif Babul,[7] S. C. Chapman[8]

[1]*Department of Physics and Astronomy, Western University, 1151 Richmond Street, London, ON, N6A 3K7, Canada*
[2]*Centre for Planetary Science and Exploration, Western University, 1151 Richmond Street, London, ON, N6A 3K7, Canada*
[3]*Harvard-Smithsonian Center for Astrophysics, 60 Garden St., Cambridge, MA 02138, USA*
[4]*Spitzer Science Center, MS 314-6, California Institute of Technology, 1200 East California Blvd, Pasadena, CA 91125, USA*
[5]*Dominion Astrophysical Observatory, National Research Council of Canada, 5071 West Saanich Road, Victoria, BC, V9E 2E7, Canada*
[6]*Department of Physics & Astronomy, The Johns Hopkins University, 3701 San Martin Drive, Baltimore, Maryland 21218, USA*
[7]*Department of Physics and Astronomy, Elliott Building, University of Victoria, 3800 Finnerty Road, Victoria, BC, V8P 5C2, Canada*
[8]*Department of Physics and Atmospheric Science, Dalhousie University, Halifax, NS, B3H 4R2, Canada*

Accepted 2016 March 14. Received 2016 March 14; in original form 2015 December 15

ABSTRACT

We present the first results from an extended survey of the Andromeda galaxy (M31) using 41.1 h of observations by *Spitzer*-IRAC at 3.6 and 4.5 μm. This survey extends previous observations to the outer disc and halo, covering total lengths of 4.°4 and 6.°6 along the minor and major axes, respectively. We have produced surface brightness profiles by combining the integrated light from background-corrected maps with stellar counts from a new catalogue of point sources. Using auxiliary catalogues we have carried out a statistical analysis in colour-magnitude space to discriminate M31 objects from foreground Milky Way stars and background galaxies. The catalogue includes 426,529 sources, of which 66 per cent have been assigned probability values to identify M31 objects with magnitude depths of $[3.6] = 19.0 \pm 0.2$, $[4.5] = 18.7 \pm 0.2$. We discuss applications of our data for constraining the stellar mass and characterizing point sources in the outer radii.

Key words: galaxies: individual (M31) – galaxies: spiral – galaxies: stellar content – infrared: galaxies

1 INTRODUCTION

Located at a distance of mere ∼ 800 kpc, the Andromeda galaxy (M31) is our closest laboratory for carrying out a 'galaxy dissection' in the Local Group. M31 ($0^h42^m44^s, +41°16'8''$) is the large galaxy for which we have the best hope of understanding all components from an external perspective, providing an important and unique comparison to models and observations of high-redshift galaxies. Recent optical surveys (Guhathakurta et al. 2006; Ibata et al. 2007, 2014) have shown that the disc and halo of M31 extend much further than previously thought, and contain stellar streams and arcs which reveal the complex history of this galaxy. The *GALEX* discovery of star-formation in outer discs (Thilker et al. 2007; Bianchi 2009), show that outer galaxy discs and halos contain important clues about disc formation, star formation, halo formation and galaxy evolution at all epochs. These clues were not accessible with previous studies of 'classical' galaxy properties within the 'optical diameter', D_{25}.

*mrafieir@uwo.ca (MRR)
†pbarmby@uwo.ca (PB)

The most recent studies (Geehan et al. 2006; Courteau et al. 2011) suggest a full three-component picture of M31, consisting of a bulge, a disc, and an extended halo. Probing the bright, crowded stellar bulge is best done in integrated light while the distant halo can be detected only with star counts. The stellar disc is probed by both the integrated surface brightness profile and star counts. The old, low-mass stars which make up the bulk of the stellar mass (Rix & Rieke 1993) have their spectral energy distribution (SED) peaks in the near-infrared band, where the effects of extinction are greatly reduced compared to visible light. This is especially important in a highly-inclined galaxy such as M31 ($i = 77°$, Corbelli et al. 2010).

Though M31 is one of the most extensively studied galaxies, many of its structural parameters remain uncertain. Near-infrared 2MASS '6x' imaging of M31 has been used to clarify the nature of M31's boxy bar and bulge (Athanassoula & Beaton 2006; Beaton et al. 2007); however 2MASS imaging is too shallow to probe the outer regions of the galaxy. While combining near-infrared data with visible light star counts is one way to bridge the gap between the inner and outer disc, such combinations suffer from uncertainty about whether the same stellar populations are being probed. Using an *I*-band composite profile, Courteau et al. (2011) computed a

Sérsic index value of $n \simeq 2.2 \pm 0.3$ for the bulge. Depending on the passbands and fitting techniques in use, disc scale lengths can vary by ~ 20 per cent. Results for the halo parameters are more promising, with a general agreement on a power-law index of -2.5 ± 0.2 (Irwin et al. 2005; Ibata et al. 2007; Tanaka et al. 2010; Courteau et al. 2011). The bulge and inner disc parameters are not independent of the outer disc and inner halo (Geehan et al. 2006). Therefore, an extended multiwavelength picture of the galaxy can help us better constrain all the parameters of the three components.

Simultaneous measurements of the outer disc and halo are extremely difficult for large galaxies observed in the ground-based near-infrared. The highly-variable near-infrared sky and the time needed to map large angular distances to a background region make background levels highly uncertain (e.g., the 2MASS Large Galaxy Atlas image of M31 is known to suffer from background subtraction problems, Barmby et al. 2006). The assumed background level can have huge effects on a derived surface brightness profile (Fingerhut et al. 2010; Sheth et al. 2010): an over-subtracted background makes the profile too steep while an under-subtracted one makes it too shallow.

Mid-infrared imaging with *Spitzer*'s Infrared Array Camera (IRAC, Fazio et al. 2004) provides a new strategy to trace the stellar mass of M31 to large radii. The efficiency of *Spitzer* in mapping large fields and the dark infrared background in space are key features not available from ground-based facilities. The mid-infrared bands trace both the integrated light of low-mass stars and bright asymptotic giant branch (AGB) stars with circumstellar envelopes, providing a unique opportunity to constrain and calibrate stellar populations in colour-magnitude space. In this paper, we present new 3.6 and 4.5 µm observations of M31 which extend to large projected distances along the major and minor axes. These data are combined with earlier observations of the M31 disc and the resulting mosaics carefully background-subtracted. The extended mosaics are used to produce a point-source catalogue and measure the surface brightness profile of the galaxy in integrated light. A statistical study of point sources in colour-magnitude space is used to extend the galaxy profile via star counts. Using the combined surface brightness profile we assess the applications of our data for finding the best physical model of the galaxy.

We adopt a distance of 785 ± 25 kpc (DM = 24.47 ± 0.07, McConnachie et al. 2005) to M31. An inclination angle of $i = 77°$ and a position angle of 37.°715 (East of North) are assumed. The Vega magnitude system is adopted with, e.g., [3.6] indicating an apparent magnitude at 3.6 µm, and $M_{3.6}$ indicating an absolute magnitude. M31-galactocentric distances are deprojected (i.e., along the major axis), unless stated otherwise.

2 OBSERVATIONS AND DATA REDUCTION

2.1 Mapping strategy and calibration

This work is based on 41.1 hrs of observations at 3.6 µm and 4.5 µm by IRAC during *Spitzer*'s warm-mission Cycle 8 with program ID (80032), between September and November 2012. Fig. 1 shows the extended regions that slightly overlap with data from Cycle 1 (Barmby et al. 2006). The total coverage of the available data is 4.°4 along the minor axis and 6.°6 along the major axis. The optical diameter of M31 is $D_{25} = 3.°4$ (de Vaucouleurs et al. 1991) so the new observations reach about $2 \times D_{25}$. The observations are summarized in Table 1.

For the observation depth, we followed the *Spitzer* Survey of

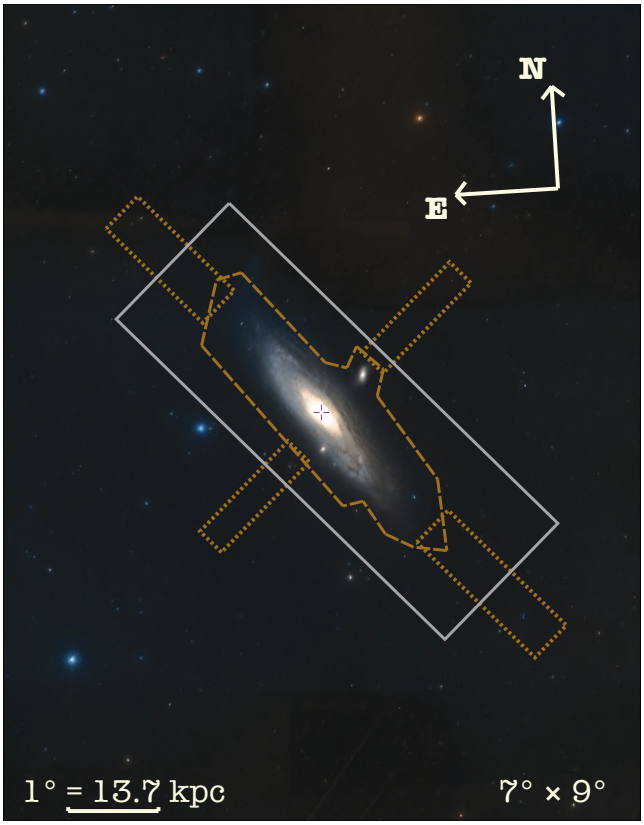

Figure 1. Digitized Sky Survey coloured map showing the extent of M31 IRAC coverage (long-dashed lines, Barmby et al. 2006), MIPS coverage (solid lines, 5.°1 × 1.°8, Gordon et al. 2006), and the extended observations (dotted lines).

Stellar Structures in Galaxies (S^{4}G, Sheth et al. 2010) and specified eight 30-second frames per sky position. This exposure time is twice that of the IRAC Cycle-1 observations of M31, which is appropriate because we were attempting to trace fainter structures. Each sky position was covered in two astronomical observation requests (AORs), each of which contained four dithered observations per position. The two AORs were observed a few hours or days apart to enable better rejection of asteroids.

The data reduction was based on Corrected Basic Calibrated Data (CBCD) files created by version S18.25.0 of the ground-system pipeline. The CBCD exposures were examined individually to exclude files compromised by scattered light and solar cosmic rays. All nominal exposures were processed using custom routines to correct column-pulldown effects arising from bright sources. The code used for this purpose, known as the "Warm-Mission Column Pulldown Corrector," is publicly available in the NASA/IPAC Infrared Science Archive (IRSA).[1]

After these preliminaries, all the 3.6 and 4.5 µm exposures were separately co-added into monolithic mosaics using IRACproc (Schuster et al. 2006). IRACproc implements the standard IRAC data reduction software (MOPEX, Makovoz et al. 2006) with a refinement that correctly handles outlier rejection in pixels having high surface-brightness gradients; this is done to account for the slightly

[1] http://irsa.ipac.caltech.edu/data/SPITZER/docs/dataanalysistools/tools/contributed/irac/fixpulldown/

Table 1. Observation Summary

Target Field (Axis)	Position (J2000)	Area	AORID	Observation Date
Major - NE	00:50:20 +43:05:00	$30' \times 90'$	42273024	2012 Oct 31
			42274048	2012 Nov 03
Major - SW	00:33:34 +39:20:00	$30' \times 90'$	42273792	2012 Oct 23
			42272768	2012 Oct 25
Minor - NW	00:48:05 +40:20:21	$20' \times 90'$	42274304	2012 Oct 22
			42273280	2012 Oct 26
Minor - SE	00:36:41 +42:47:20	$20' \times 105'$	42273635	2012 Sep 22
			42274560	2012 Sep 22

under-sampled IRAC point spread function in 3.6 and 4.5 μm passbands. The software was configured to automatically flag and reject cosmic ray artefacts. The output mosaics were generated with 1.″2 pixels, close to the native IRAC pixel scale. This scale slightly under samples the angular resolution of the telescope and instrument at these wavelengths (1.″8). Each mosaic was paired with an associated coverage map that indicated the number of IRAC exposures used to construct each mosaic pixel. Because of limitations imposed by computer memory, two sets of mosaic-coverage-map pairs were generated. One set was aligned with the galaxy major axis, covering a narrow strip $50' \times 6.^{\circ}5$ centred on M31. The other set was aligned with the galaxy minor axis, covering an overlapping orthogonal strip $25' \times 5^{\circ}$. Combining the IRAC exposures from the warm and cryogenic missions thus results in continuous coverage of both the major and minor axes of this galaxy that extends several scale lengths beyond the visible galaxy disc. Because of dithering, combination of data from multiple AORs, and the offset fields of view in the two bands, the depth of observations varies with location in the final mosaic. The central region of the galaxy covered with 6×12 s exposures extends for approximately 100′ on the major axis; beyond this, the outer part of the Cycle 1 observations, with 4×30 s exposures, extends for ∼ 50′ to North and South; the area covered in the new observations, with 8×30 s exposures, extends for ∼ 80 - 90′ again to both North and South.

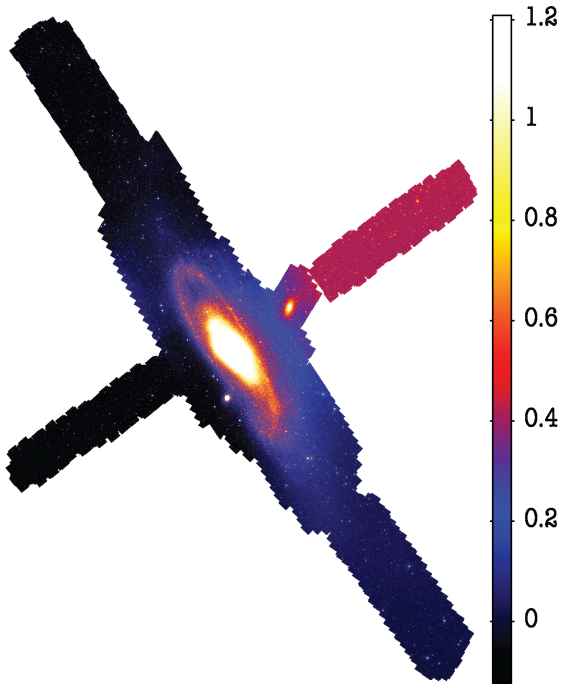

Figure 2. Calibrated raw mosaic of M31, observed at 3.6 μm during the cryogenic and warm cycles of *Spitzer*-IRAC. North points up and East is towards left. The colourbar [MJy sr^{-1}] is constrained and scaled to show background variations. MONTAGE (Jacob et al. 2009) was used for stitching the two minor- and major-axis mosaics.

2.2 Flux uncertainty estimation

As part of the main pipeline, mosaics were corrected for the instrument bias and the (much smaller) dark current. It was assumed that all of the darks are noise-free, and the non-linear background is entirely due to the zodiacal light (Krick et al. 2012). An absolute calibration uncertainty is computed by multiplying an estimate for the zodiacal light, provided in the BCD header as `ZODY_EST`, by the extended-to-point source calibration ratios (with 10 per cent uncertainty) given in the IRAC Instrument Handbook. The value of `ZODY_EST` is computed by a model with 2 per cent uncertainty. Based on the upper limits of `ZODY_EST` in a few randomly picked BCD images over the entirety of observed fields, we found absolute calibration uncertainty values of $\sigma_{zod} = 0.0014$ and 0.006 MJy sr^{-1} at 3.6 and 4.5 μm, respectively. The combined uncertainty value of a given pixel is therefore $(\sigma_p^2 + \sigma_{zod}^2)^{1/2}$, where σ_{zod} is in electron counts and σ_p is the Poisson noise associated with random photons.

2.3 Background subtraction

Accurate background subtraction is critical for surface photometry at faint levels. The 'first-frame effect' in the IRAC detectors combines with the instrument's lack of a shutter to make background levels highly uncertain. Background-matching on local scales in the mosaicing process can induce significant gradients in background over large scales (Arendt et al. 2010). Fig. 2 shows the large background gradient in the 3.6 μm raw mosaic; this gradient, if unsubtracted, would swamp any signal from the low-surface-brightness outer disc. To model the background, mosaic regions covered by M31 and its satellites were heavily masked up to where point sources could be distinguished from one another (i.e., uncrowded regions). Source Extractor (SExtractor, Bertin & Arnouts 1996) was used to locate point sources and other background discontinuities for further masking. SExtractor parameters were fine-tuned by visual inspection so that a significant number of regions were masked – see section 3.1 for a full discussion on the robust detection and photometry of IRAC sources using SExtractor.

Using mosaics where galaxies and other sources were masked, background maps were produced as follows. A median value was computed in square regions of 100×100 pixels that ultimately cover the full mosaics. Fully-masked regions were assigned an average value based on the median in their neighbouring regions. Then, all pixels were replaced with corresponding median values in their

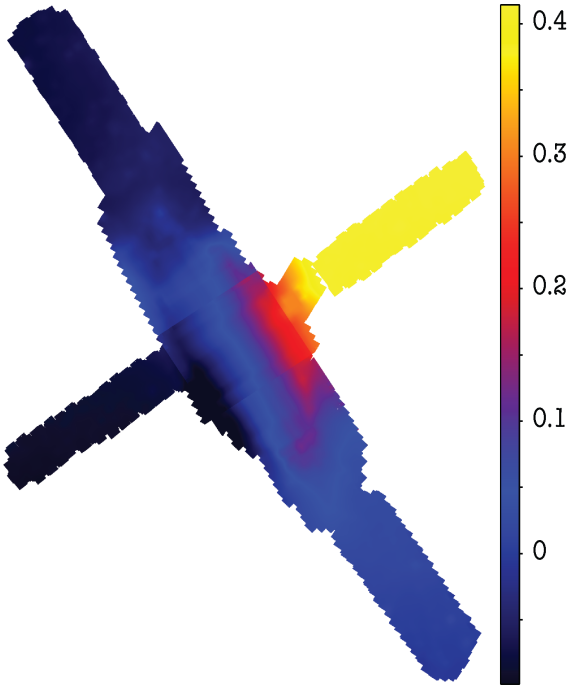

Figure 3. Background model at 3.6 μm . North points up and East is towards left. The colourbar [MJy sr^{-1}] is constrained and scaled to show background variations.

region. The galaxy, masked by an ellipse, was assumed to follow a first-degree polynomial over rows and columns. Straight lines were fit to end points along the rows and columns, hence across the elliptical mask over the galaxy. The background maps were smoothed by taking the average value in a moving box of 199×199 pixels. Finally, the smoothed maps were subtracted from the calibrated mosaics. Fig. 3 shows the 3.6 μm background model which is very similar to that for the 4.5 μm background. The raw mosaics and modelled background images will be available at `http://irsa.ipac.caltech.edu/data/SPITZER/M31IRAC`.

3 IRAC CATALOGUE

3.1 IRAC catalogue construction

The extended IRAC maps contain a wealth of information not only in the pixel-by-pixel light variation but also through distinct properties of point sources. Point sources in the mosaics were extracted using SExtractor in dual-image mode, with the 3.6 μm image used for detection; the 3.6 and 4.5 μm images were used for photometry. Point sources were extracted on the mosaics before the background modelling and subtraction described in section 2.3; large-scale background subtraction should not affect point-source photometry since SExtractor determines the background local to each object. Input parameters for SExtractor were set through experimentation and visual inspection, with the final values given in Table 2.

SExtractor could not process the full mosaic images due to memory limitations, so we ran it on sub-sections of the mosaics (larger sub-sections in the uncrowded outer regions, and smaller sub-sections closer to the disc) and combined the resulting sub-catalogues. The coverage images generated during mosaicing were used as 'weight maps' input to the SExtractor detection procedure, such that a faint object appearing on a deeper area of the image receives greater weight than one on a shallower area. The area measured includes all of the area covered by the Cycle 8 data as well as some of the disc region from the Cycle 1 observations.

Table 2. Parameter settings for SExtractor

Parameter	Value
`DETECT_MINAREA` [pixel]	3
`DETECT_THRESH`	1.0
`FILTER`	Y
`FILTER_NAME`	`gauss_1.5_3x3.conv`
`DEBLEND_NTHRESH`	64
`DEBLEND_MINCONT`	0.0001
`SEEING_FWHM` [arcsec]	1.66
`GAIN`	0.0
`BACK_SIZE` [pixel]	64
`BACK_FILTERSIZE`	3
`BACKPHOTO_TYPE`	`LOCAL`
`BACKPHOTO_THICK`	24
`WEIGHT_TYPE`	`MAP_WEIGHT`

Photometry with SExtractor was performed in circular apertures of radius 1.″5, 2.″0, 2.″5, 3.″0, and 6.″0 as well as in the `AUTO` and `ISOCOR` system. Because SExtractor's photometric uncertainties do not account for correlated noise between mosaiced pixels, we account for this by multiplying the uncertainties by a factor of two, as in Boyer et al. (2015).

3.2 Catalogue description

The IRAC M31 catalogue is presented in Table 3.[2] To avoid noisy regions near the edges, only mosaic regions with coverage ≥ 2 images per sky position at 3.6 μm were used to generate the catalogue. This is a total area of about 15,631 arcmin^2 (4.342 deg^2). The catalogue contains 426,529 point sources detected at 3.6 μm of which 423,588 are also detected at 4.5 μm. Aperture corrections were derived from Ashby et al. (2009) and are also given in Table 4. The magnitude uncertainties given do not include systematic calibration uncertainty (2 per cent; Reach et al. 2005). The saturation limits for 30-second frames are 10 and 12 mJy in 3.6 and 4.5 μm bands (Spitzer Science Center 2015), or $m_{\rm Vega} = 11.1$ and 10.4, respectively. The analysis in the remainder of this paper uses IRAC aperture magnitudes, measured in a 2″ radius aperture, large enough to contain a majority (∼ 60 per cent) of the light from point sources but not so large as to inflate the photometric noise from background; in addition, all used point sources (including those in auxiliary catalogues) have magnitude uncertainties of less than 0.2.

3.3 Completeness

Catalogue completeness was analysed through the usual 'artificial star' method on the 3.6 μm mosaics. A point-spread function (PSF) was simulated by making cutout images of about 90 bright ($13 \gtrsim [3.6] \gtrsim 11$), isolated stars from the mosaic, scaling the images to the same total flux, and co-adding them weighted by star magnitude. Although the PSF varies over the mosaic due to the spatially-varying depth and position angle, we verified that the completeness results are not strongly dependent on the exact PSF shape. Artificial stars were inserted into the mosaic images, SExtractor was run on

[2] Also available at `http://irsa.ipac.caltech.edu/data/SPITZER/M31IRAC`.

Table 3. IRAC M31 catalogue column definitions. This table will be available in its entirety in a machine-readable form at http://irsa.ipac.caltech.edu/data/SPITZER/M31IRAC. A portion is shown here for guidance regarding its form and content.

Column	Parameter	Description	Units
0	ID	M31IRAC JHHMMSS.ss+DDMMSS.s	
1	Number	Running object number	
2	KRON_RADIUS	Kron apertures in units of A or B	
3	A_IMAGE	Profile RMS along major axis	[pixel]
4	X_IMAGE	Object position along x	[pixel]
5	Y_IMAGE	Object position along y	[pixel]
6	X_WORLD	Barycenter position along world x axis	[deg]
7	Y_WORLD	Barycenter position along world y axis	[deg]
8	ALPHA_J2000	Right ascension of barycenter (J2000)	[deg]
9	DELTA_J2000	Declination of barycenter (J2000)	[deg]
10	ELLIPTICITY	1 − B_IMAGE/A_IMAGE	
11	FWHM_WORLD	FWHM assuming a Gaussian core	[deg]
12	CLASS_STAR	S/G classifier output	
13	FLAGS	Extraction flags	
...	MAG_AUTO_i	Kron magnitude	Vega mag
...	MAGERR_AUTO_i	Kron magnitude uncertainty	Vega mag
...	MAG_APER_i	ap mags: 1.″5, 2″, 2.″5, 3″, 6″ radii	Vega mag
...	MAGERR_APER_i	aperture magnitude uncertainties	Vega mag
...	MAG_ISOCOR_i	isophotal mag above det threshold	Vega mag
...	MAGERR_ISOCOR_i	isophotal magnitude uncertainty	Vega mag
...	FLUX_AUTO_i	Kron flux	μJy
...	FLUXERR_AUTO_i	Kron flux uncertainty	μJy
...	FLUX_APER_i	ap flux: 1.″5, 2″, 2.″5, 3″, 6″ radii	μJy
...	FLUXERR_APER_i	aperture flux uncertainties	μJy
...	FLUX_ISOCOR_i	corrected isophotal flux	μJy
...	FLUXERR_ISOCOR_i	isophotal flux uncertainty	μJy
...	...	...	
78	P(M31)	Probability for being M31 object	
79	N_ROBUST	Robust count = $P(M31) \times (\text{Completeness})^{-1}$	
80	R_PROJ	Projected galactocentric distance	[arcmin]
81	R_DEPROJ	Deprojected galactocentric distance	[arcmin]

Table 4. Aperture corrections for M31 IRAC mosaics – corrections to be added to aperture magnitudes to convert them to total magnitudes.

Band	Aperture radius				
	1.″5	2.″0	2.″5	3.″0	6.″0
3.6	−0.67	−0.38	−0.24	−0.17	0
4.5	−0.69	−0.40	−0.25	−0.17	0

the resulting images in the same manner as for the real source, and the artificial stars identified in its output based on their known input positions. About 83,000 artificial sources were inserted at random positions in the same regions of the major- and minor-axis mosaics used for analysis, with a power-law ($\alpha = 0.3$) distribution of magnitudes in the range $14 < [3.6] < 22$. The artificial stars were inserted 5,000 at a time in the uncrowded outer regions of the mosaic, and 500 at a time in the inner regions, following the same subregion procedure as for the real catalogue. An artificial star was considered to be detected if its SExtractor-measured position was within a distance of 1.5 pixels from the input position. To account for the effects of crowding, artificial objects were also required to be more than 2.″5 from any real catalogue sources, and have magnitudes within 1.0 mag of the input value, to be considered detected.

Fig. 4 shows the completeness estimates derived by sorting the artificial sources into bins by input magnitude and projected galactocentric distance, then dividing the number of recovered sources by the number input in each bin. As expected, the completeness declines as artificial objects become fainter and/or closer to the galaxy disc. Even for the brightest sources, the catalogue is not 100 per cent complete, because a bright artificial star can randomly fall too close to another bright source to be a separate detection. The 50 per cent completeness limit is $[3.6] = 18.5$ at R = 17′ and $[3.6] = 21.3$ at R = 180′, where radial distances are projected. Testing SExtractor's photometry by comparing input and recovered magnitudes, we found that the offsets between input and output magnitudes were consistent with zero. The exception is in the innermost bins of projected galactocentric distance, where output magnitudes were brighter than input, presumably due to the effects of crowding. We have not attempted to quantify the reliability of the catalogue (i.e., the fraction of spurious noise-induced sources) as we believe that crowding-induced incompleteness is likely to be a much larger effect than noise spikes being mistaken for real sources.

3.4 Checks on astrometry and photometry

Cross-matching with other catalogues is one way to characterise the photometric and astrometric precision and accuracy of the IRAC catalogue. The *WISE* All-Sky Survey (Wright et al. 2010) included the Andromeda region at 3.4 μm ($W1$), 4.6 μm ($W2$), 12 μm ($W3$) and 22 μm ($W4$) with angular resolutions of 6.″1, 6.″4, 6.″5, 12.″0, and its catalogue of point sources is publicly available in the IRSA[3]. *WISE* detection limits are $W1 < 15.3$, $W2 < 14.4$, $W3 < 10.1$ and

[3] http://irsa.ipac.caltech.edu/cgi-bin/Gator/nph-scan?mission=irsa&submit=Select&projshort=WISE

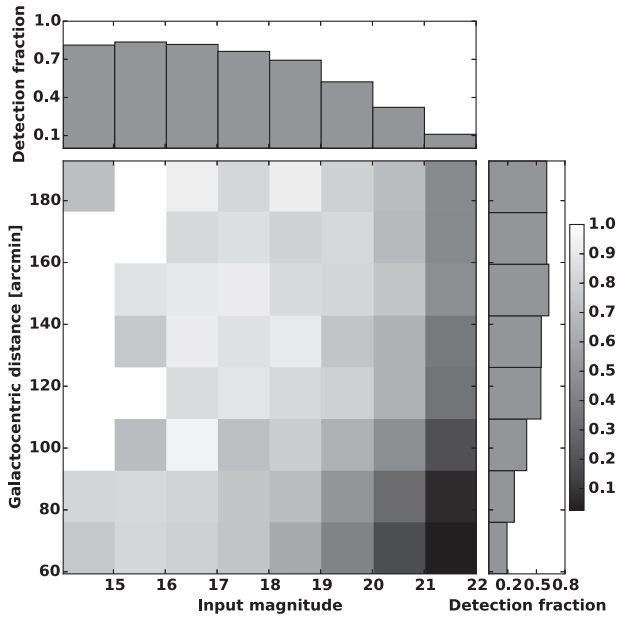

Figure 4. Completeness for M31 IRAC catalogue, as derived from artificial star tests on the 3.6 µm major-axis mosaic. Completeness is defined as the fraction of input objects in a given bin of location (projected galactocentric distance) and 3.6 µm magnitude detected within 1.5 pixels and 1.0 magnitude of the input values, and not found within 2.″5 of a real catalogue source. Histograms at top and right show the two-dimensional completeness histogram summed along the other dimension. A similar analysis (not shown) was carried out for the catalogue of sources on the 3.6 µm minor-axis mosaic.

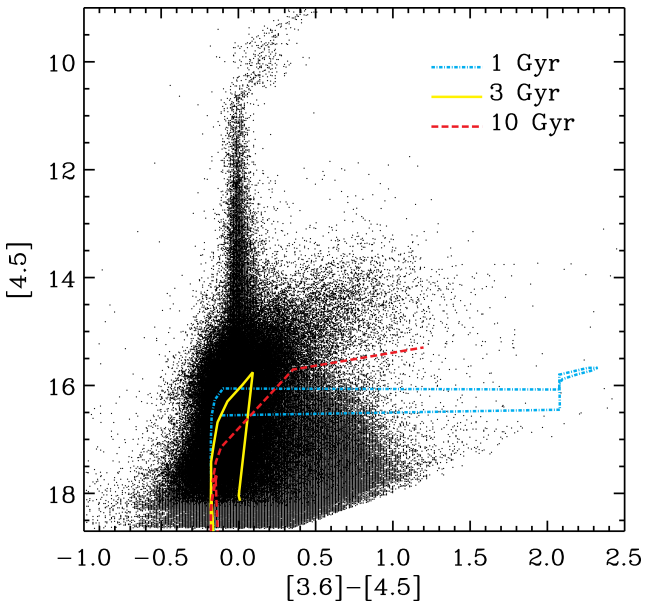

Figure 5. The mid-infrared CMD of IRAC sources overlaid with isochrones from Marigo et al. (2008). A metallically of $Z = 0.016$ is assumed for ages of 1, 3, and 10 Gyr. The red plume of objects at $[3.6]-[4.5] \simeq 1$ are likely to be associated with M31. The horizontal branch at $[4.5] < 10$ is artificial and due to the saturation limits of the IRAC passbands. Faint objects beyond $[3.6]-[4.5] > 1$ are likely to be red background galaxies. All point sources have magnitude uncertainties of less than 0.2.

$W4 < 6.7$ Vega mag at SNR = 5. We obtained an IRAC/*WISE* catalogue of point sources by finding best matches within a 2″ radius.

With its larger point-spread function, *WISE* data will be more affected by crowding than IRAC, so we carry out the following comparisons only in the outer regions (where $R_{deproj} > 110'$) of the IRAC dataset. Our matching of IRAC and *WISE* sources shows that the mean and standard deviation of the separation between matched sources is 0.″1 ± 0.″4 in RA and Dec. This is consistent with the expected IRAC positional uncertainties (Spitzer Science Center 2015) and indicates that the mosaicing process did not substantially worsen the astrometry. In uncrowded fields *WISE* photometry $W1$ and $W2$ has been shown to be within 3 per cent of IRAC 3.6 and 4.5 µm (Jarrett et al. 2011). We compared aperture photometry for all matched, non-saturated IRAC objects with $11 < [3.6, 4.5] < 15$, and found mean and standard deviation of photometric offsets (IRAC−*WISE*) 0±0.01 mag in both bands. Photometry on the IRAC mosaics is therefore inferred to be reliable.

4 SOURCE CHARACTERIZATION

4.1 Catalogue object properties

We now explore the properties of the individual point sources detected in the M31 mosaics. Three classes of objects are expected to dominate the population: foreground Milky Way (MW) stars, bright M31 stars, and background galaxies. Boyer et al. (2015) give a detailed discussion of the stellar populations that dominate the resolved 3.6 and 4.5µm light: both red giants and asymptotic giant branch stars are important. While the spectral energy distribution of most stars is Rayleigh-Jeans in the 3.6 and 4.5µm bands and thus their Vega-magnitude colours are $[3.6]-[4.5] \sim 0$, stars with circumstellar dust can have colours as red as $[3.6]-[4.5] \sim 1.0$. The brightest M31 objects are expected to be AGB stars with an absolute magnitude of $M_{3.6}^{AGB} = -10.3$ (Boyer et al. 2009). This translates into an apparent magnitude of $[3.6] \geq 14.1$, which we choose as the bright magnitude limit for potential M31 objects through the rest of our analysis. The tip of the red giant branch in M31 is expected to be about 4 magnitudes fainter than the brightest AGB stars (Boyer et al. 2015), or $[3.6] \approx 18$. Foreground Milky Way dwarf stars are expected to be dwarfs with $[3.6]-[4.5] \sim 0$ (and see section 4.3).

Background galaxies are expected to have a broad range of colours and magnitudes; background galaxy colours and luminosity functions can be estimated by comparison with blank-field extragalactic surveys. The brighter background galaxies can be identified with the SExtractor `CLASS_STAR` output variable (Barmby et al. 2008). Selecting sources with $[3.6] < 15$ and `CLASS_STAR` < 0.05, we identified approximately 3,882 potential galaxies in the catalogue. Further discussion of background galaxies is found in section 4.4; as these sources are not the focus of this work, we have not attempted to analyse them in detail (e.g., by measuring shapes or applying extended source photometric corrections).

Fig. 5 shows the colour-magnitude diagram (CMD) of the IRAC catalogue overlaid with isochrones from Marigo et al. (2008)[4] with the corrections from Case A in Girardi et al. (2010), bolometric corrections from Aringer et al. (2009) and Chen et al. (2014), and circumstellar dust models from Groenewegen (2006).

[4] http://stev.oapd.inaf.it/cgi-bin/cmd

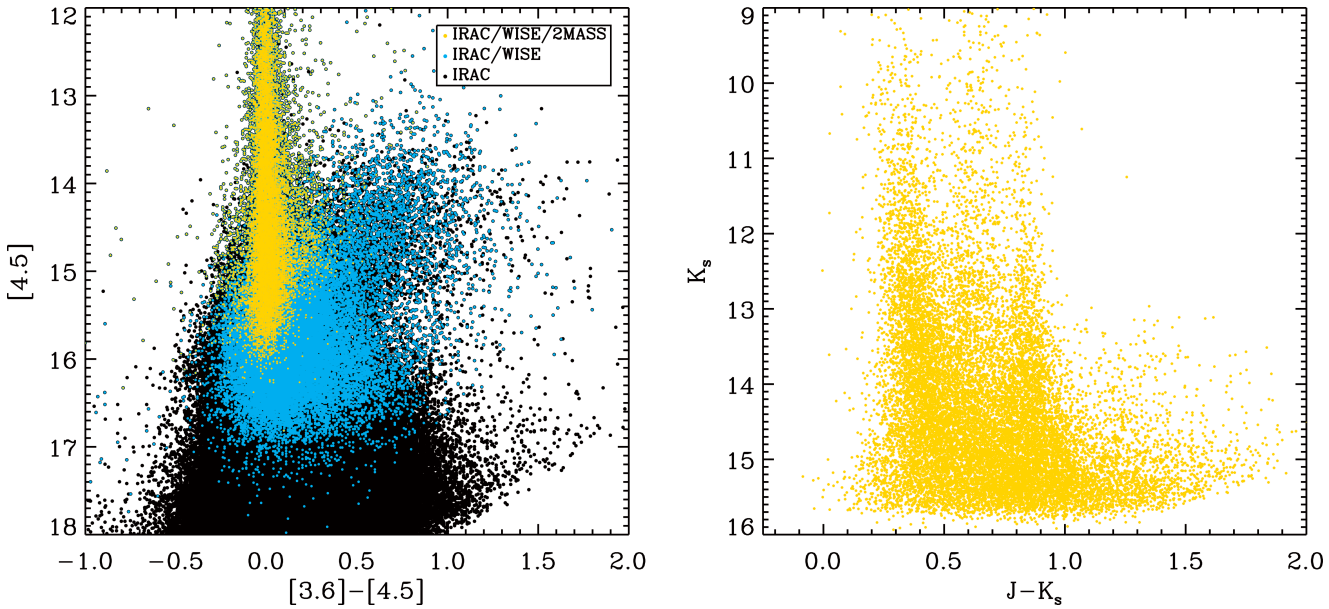

Figure 6. Colour-magnitude diagrams of cross-matched IRAC/*WISE* point sources with a tolerance of 2″ . Black points in the background show (un)matched sources in the IRAC catalogue. All point sources have magnitude uncertainties of less than 0.2. Left: IRAC-band CMD. Right: Near-infrared (2MASS) CMD of IRAC/*WISE* sources that also have robust counterparts in the 2MASS catalogue.

We use the default values: a metallicity of $Z = 0.016$ coupled with a circumstellar dust composition of 60 per cent silicate and 40 per cent AlOx (amorphous porous Al_2O_3) are assumed for ages 1, 3, and 10 Gyr. The total extinction is assumed to be zero. Most of the stars and isochrones are concentrated around the [3.6]−[4.5] ∼ 0 colour; however, a redder branch predicted in the 10 Gyr isochrone is also apparent in the data.

4.2 Multi-wavelength identification

The Andromeda neighbourhood has been well-observed in other passbands using both ground- and space-based telescopes, providing the opportunity for cross-correlation and identification of sources. When comparing the IRAC photometry with other measurements it should be kept in mind that bright AGB stars often are photometric variables, with amplitudes of a magnitude or more. If the photometry is not recorded at the same epoch then agreement will suffer as stars near the faint limit move in and out of detectability. This is likely to be of greatest concern for the reddest AGB stars when making comparison with visible-light observations, which will be biased against detecting the reddest, most evolved stars due to line blanketing effects and obscuration by circumstellar discs. Even for variable stars which are well-detected with IRAC, the combination of the instrument's offset fields of view and the observing strategy means that 3.6 and 4.5 µm observations of a given object are generally not simultaneous. This will introduce additional scatter into the colours of variable sources.

Cross-matching between IRAC and the *WISE* All-Sky Survey was introduced in section 3.4. 15 per cent of IRAC sources have robust (i.e., sources with magnitude uncertainties of less than 0.2) *WISE* counterparts over our extended observations. 37 per cent of IRAC/*WISE* sources also have robust matched counterparts from the Two Micron All-Sky Survey (2MASS, Skrutskie et al. 2006), which operated at 1.25 µm (J), 1.65 µm (H), and 2.17 µm (K_s) with an angular resolution of 2″ in each of the three bands. 2MASS detection limits are $J < 15.8$, $H < 15.1$ and $K_s < 14.3$ Vega mag at SNR = 10. Fig. 6 shows colour-magnitude diagrams of cross-matched IRAC/*WISE* point sources.

The *WISE* dataset is relatively shallow, and comparison with a deeper mid-infrared survey can give insight into the types of objects present in the M31 catalogue, including contaminating foreground and background sources (see sections 4.3 and 4.4). Visually inspecting and comparing our M31 CMD to that from M33 observations by McQuinn et al. (2007), we identified the two main populations of M31 objects in mid-infrared: oxygen-rich giant and carbon stars with approximate mean [3.6]−[4.5] colours of −0.1 and 0.3, respectively. While the 'blue' giants are more numerous, the redder carbon stars contain a significant number of variable stars – McQuinn et al. (2007) reported 34 per cent for the red plume of objects in the M33 CMD.

The Pan-Andromeda Archaeological Survey (PAndAS, McConnachie et al. 2009) covered over ∼ 400 deg^2 of the Andromeda neighbourhood using CFHT/MegaCam in g (4,140 – 5,600 Å) and i (7,020 – 8,530 Å) passbands with mean resolutions of 0.″67 and 0.″60, respectively. The PAndAS catalogue has median 5σ detection limits of 26.0 and 24.8 Vega mag in the g and i bands, respectively. Fig. 7 shows the CMD of PAndAS sources that have (not) been matched to IRAC sources within a 1″ radius; IRAC sources are clearly centred around two lobes in the red regime, indicating very mid-infrared-bright objects (e.g., giant stars and background galaxies) that extend their SED to the visible regime.

4.3 Estimating contamination: Milky Way stars

Tracing the light of M31 requires a careful treatment of all possible sources of contamination due to the foreground Milky Way stars as well as background galaxies. While all-sky surveys can be helpful in estimating the contribution from foreground objects at a given Galactic latitude, there still remains the possibility of cross-contamination from the M31 halo. This unwanted effect can be mitigated by choosing foreground samples well outside the halo. Using the *WISE* All-Sky Survey and TRILEGAL (v1.6, Girardi et al. 2005)

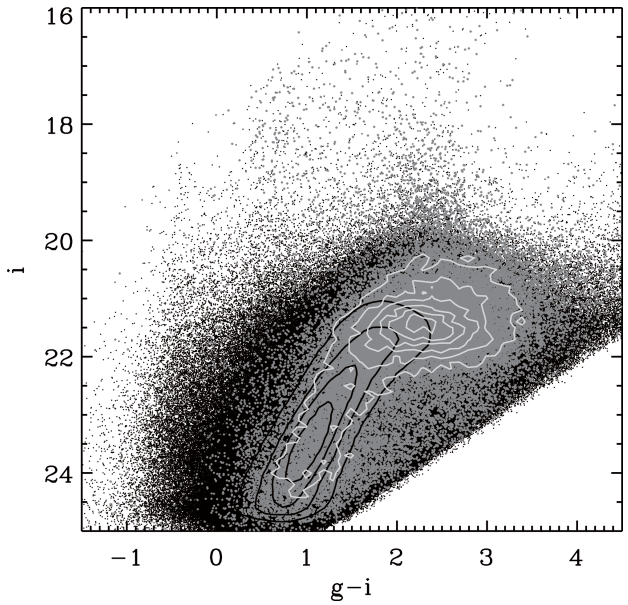

Figure 7. CMD of cross-matched point sources with a tolerance of 1″ in the visible regime. The selected auxiliary (PAndAS, in black) coverage is slightly larger than the full IRAC (in grey) observations. The linear contours are to illustrate number density variations using a CMD bin size of 0.1×0.1.

stellar population models we obtained the probability (Bagheri et al. 2013) that a point source would belong to M31, by comparing to the number density of foreground stars:

$$P(M31) = \frac{N_{M31} - N_{MW}}{N_{M31}} \qquad (1)$$

where N is the number of stars in a CMD bin. Highly contaminated bins with $N_{MW} \geq N_{M31}$ were assigned a probability value of zero; thus, $0 \leq P(M31) \leq 1$. Using the *WISE* catalogue we selected two $1^\circ \times 1^\circ$ foreground regions at ($23^h29^m20^s$, $+37^\circ46'35''$) and ($03^h08^m03^s$, $+32^\circ26'10''$), which are well outside our extended IRAC coverage but within $-22^\circ \leq b \leq -21^\circ$. We linearly scaled their number densities according to the total area covered by the IRAC observations. Assuming a homogeneous distribution of Milky Way stars along the same Galactic latitude, our foreground fields are representative samples of stellar populations in the M31 neighbourhood. Using these foreground regions and the matched IRAC/*WISE* catalogue, we used equation (1) to compute probability values in CMD bins with $[4.5] \leq 16$. This approach is independent of the instruments' detection efficiencies as it only involves matched point sources between the two catalogues. The *WISE* catalogue does not provide a statistically robust sample of objects for bins fainter than $[4.5] \sim 16$.

To model the fainter foreground stars, we used stellar population models to estimate the distribution of MW stars with $[4.5] > 16$ at the position of M31. Using the same extended IRAC coverage we generated a TRILEGAL run with default values. Next, model magnitudes were smoothed by adding a Gaussian noise from the IRAC uncertainties – we chose a magnitude bin width of 0.2 and computed the mean of uncertainties in each bin. Observed colour values are more uncertain than magnitude values because they combine two measurements; for the colour width of the bins we chose a value of 0.8. While this is fairly large compared to the CMD width, it ensures that each bin includes a statistically robust sample of stars and suppresses the scatter due to variable stars, while still mapping visually separable features in the colour-magnitude space (see, e.g., figure 15 of McQuinn et al. 2007). Using the modified TRILEGAL catalogue equation (1) was used to estimate $P(M31)$ for bins with $[4.5] > 16$. In this analysis, the faintest objects with magnitude uncertainties of less than 0.2 have $[4.5] \approx 18.7$.

4.4 Estimating contamination: background galaxies

Another source of contamination is the uniform distribution of background galaxies in mid-infrared. Our foreground estimation technique using the *WISE* catalogue accounts for the contribution from background galaxies with $[4.5] \leq 16$. In addition, we selected *stellar* objects by removing sources with $[3.6] < 15$ and CLASS_STAR < 0.05 from the IRAC catalogue. The selection criteria for *stellar* objects combined with colour-magnitude uncertainties produced bins with probability values of greater than 1, which were subsequently normalised to 1.

Nevertheless, these criteria fail to identify galaxies fainter than $[3.6] \sim 16.5$ as they are primarily undetected by *WISE* and also exhibit the same IRAC magnitudes (within the uncertainty range) in all apertures. For bins with $[4.5] > 16$, we made use of the Spitzer Deep, Wide-Field Survey (SDWFS, Ashby et al. 2009) to statistically measure the abundance of background galaxies in the colour-magnitude bins. Using the IRAC instrument and observing ~ 10.5 deg^2 of a relatively foreground-free region at ($l = 57.^\circ5, b = 67.^\circ5$), the SDWFS has sufficient depth and coverage to provide a statistically robust sample of background galaxies. Removing the contribution due to any foreground stars, we generated a TRILEGAL model (with default values) over a 10 deg^2 field, at the SDWFS sky position. Number densities were scaled by the SDWFS coverage and a Gaussian noise was applied to the magnitudes based on the SDWFS magnitude uncertainties. Using the same bin size and replacing N_{MW} by background galaxy number counts[5], equation (1) was applied to find the probability that a source would belong to MW *or* M31. Multiplying the foreground (based on TRILEGAL simulations of M31 field) by the background (based on foreground-free SDWFS) probabilities, we combined the statistics for sources with $[4.5] > 16$.

The result is shown in Fig. 8. Attempting to select distinct populations of objects, separated by different colours in multiple datasets, resulted in some sharp discontinuities along the colour axis (i.e., constant [4.5]) – this is in contrast to the relatively smooth probability variation along the densely-packed magnitude axis. As discussed in section 4.3, using smaller colour bins would have introduced other problems, such as variability-induced scatter. Because of the complexity and uncertainty associated with the inclusion of multiple auxiliary catalogues, we refrained from propagating uncertainties in our pipeline; thus, we did not attempt to smooth out the colour jumps in the CMD. We remind the reader that this is a probabilistic colour-magnitude diagram based on photometry; we have not attempted to use radial velocities or other cross-identifications to assess M31 membership probabilities.

4.5 Contamination-corrected catalogue

After removing bright foreground stars and resolved background galaxies, our M31 catalogue contains 279,509 sources with magnitude depths of $[3.6] = 19.0 \pm 0.2$ and $[4.5] = 18.7 \pm 0.2$. We assigned $P(M31)$ values to each object based on its location in

[5] In SDWFS colour-magnitude bins, the background galaxy count is given by subtracting the foreground (TRILEGAL) from the total count.

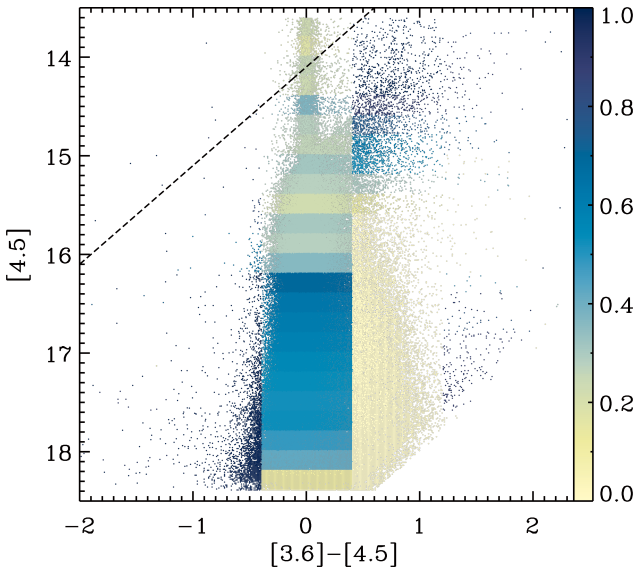

Figure 8. The mid-infrared CMD of IRAC sources. The colour-bar represents the probability for a source to belong to M31. The dashed line shows the AGB cut, defined by the brightest AGB stars at the distance of M31. Objects with [3.6] < 14.1 (i.e., above AGB cut) are assumed to be foreground Milky Way stars. Highly probable M31 carbon stars coalesce into a clump with [4.5] ≳ 15 and [3.6]−[4.5] ≳ 0.4. The fainter area under this region is severely contaminated by star-forming background galaxies. The central branch at [3.6]−[4.5] ∼ 0 contains a blend of all sources, including a large population of Milky Way dwarf stars.

the M31 CMD. These objects cover a wide range of projected galactocentric radii between 5.′4 (22.′9 deprojected) and 200.′6 (637.′4 deprojected). We found an average probability value of $P_{\rm avg}(M31) = 0.4 \pm 0.2$, where the uncertainty is empirically based on the variation of probability values in colour-magnitude space. Cross-matching with other catalogues, we found that the potential M31 sources were robustly matched with 35,437 and 51,574 *WISE* and PAndAS catalogue sources, respectively. Future work will analyse this rich dataset in detail. In section 5.2, we use the contamination-corrected catalogue to measure number density variations in the disc and halo of M31.

5 SURFACE BRIGHTNESS PROFILE

A typical overall approach to determining galaxy surface brightness profiles is to measure integrated light closer to the centre and combine that with star counts in the outer part. Our large mosaics allow us to perform both measurements for M31 on the same dataset. The robustness of both background subtraction and catalogue construction can be tested by comparing the two methods in the radial region where they overlap.

5.1 Integrated light

We traced the integrated light by computing the median value in width-varying elliptical bins while keeping the inclination and position angle constant. We used equation (2) (Courteau et al. 2011) to determine the exponentially increasing width (w) of the elliptical bins:

$$w = p\,(r^n - 1) \qquad (2)$$

where n is the bin number starting at 0, $p = 5.'25$ and $r = 1.01$ are fine-tuning constants – these values produce statistically robust samples for tracing the light over size-varying galactic structures (e.g., the 10 kpc ring). Measuring the flux from M31, we masked out the satellite galaxy NGC 205 with a square on the minor-axis mosaic.

In each elliptical bin, we obtained a distribution of median values by bootstrapping 100 times over all unmasked pixels. The bootstrapping was done by sampling a bin's pixels (with replacement) and finding the median for each resampled bin. A final median value and its uncertainty were given by the mean and standard deviation of the corresponding distribution for each bin. To best mitigate possible contamination from bright point sources, pixels above $+3\sigma$ level were clipped, and the median was recomputed along with its associated uncertainty. Furthermore, we computed the uncertainty associated with extreme cases of the background model from section 2.3. In each bin, we summed the two (i.e., the final standard deviation from bootstrapping and the absolute difference from extreme cases of the background) uncertainties in quadrature. We did *not* use the absolute uncertainty from section 2.2. The current implementation robustly accounts for much larger uncertainties due to the background and the pixel counts.

For bins larger than 5′ in diagonal, median flux values were multiplied by the extended-to-point source calibration ratios (with a 10 per cent uncertainty) given in the IRAC Instrument Handbook. Surface brightness in [MJy sr^{-1}] was converted to [mag arcsec^{-2}] by the following transformation: $\mu = \mu_\circ - 2.5 \log(I)$, where μ and I are in [mag arcsec^{-2}] and [MJy sr^{-1}], respectively; $\mu_\circ = 17.30$ and 16.81 [mag arcsec^{-2}] are in the Vega photometric system at 3.6 and 4.5 μm passbands, respectively.

As a result of uncertainties in the background, bins in $86' < R < 90'$ produced unreliable measurements; bins beyond R ∼ 90′ contained negative median-flux values, resulting in undefined logarithmic values for the magnitude. We used the distribution of point sources as a light tracer in the outer radii.

5.2 Star counts

When the integrated-light profile approaches the background level, surface brightness measurements become uncertain. In this case, star counts can be used as a tracer of the galaxy light. The inclined distribution of M31 giants inside R = 55 kpc (see fig. 1 in Tanaka et al. 2010) motivates us to explore number counts in the deprojected bins. To this end, we counted the number of *stellar* objects (see section 4.4) within the width-varying elliptical annuli from R = 90′ (20.6 kpc) out to R = 200′ (45.7 kpc) – the distribution of sources outside this range is uncertain due to crowding (in the inner regions) and sparsity (in the outer regions). The elliptical bin width (w) was computed by equation (2) with $p = 3.'1$ and $r = 1.1$; these values provide large counts with small uncertainties for tracing the faint light. In this work, we only used objects with [3.6]−[4.5] > −0.75; bluer objects are not physically reliable. The probability values of sections 4.3 and 4.4 were included in this analysis, suppressing the contamination due to the foreground MW stars and background galaxies. Giving a larger weight to *potential* M31 objects, we only considered sources with $P(M31) \geq 0.5$; all other sources with $P(M31) < 0.5$ were ignored while computing the total counts. In addition, we corrected the counts for incompleteness; the two-dimensional (in magnitude and projected galactocentric distance; see Fig. 4) completeness results were applied, with the same bin parameters as in section 3.1, to sources detected on the minor- and major-axis mosaics.

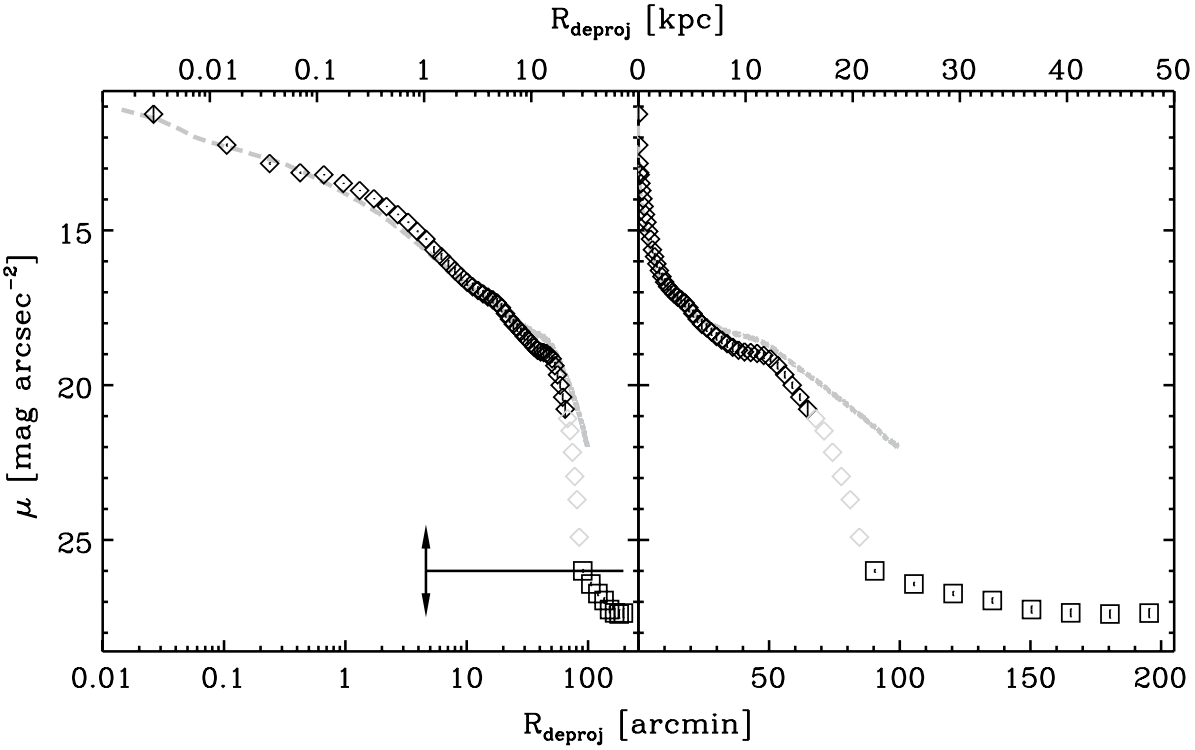

Figure 9. M31 surface brightness profiles based on a combination of surface photometry at 3.6 μm (diamonds) and the radial distribution of stars (squares) over the entire IRAC observations. The grey dashed line shows an azimuthally averaged profile by Courteau et al. (2011). Panels contain identical measurements; a logarithmic axis is used for probing R < 20′ in the left panel. The horizontal bar marks $\mu = 26$, which is an arbitrary value (thus shown by arrows) that we chose for the first bin computed by star counts; the following bins were shifted by the same offset. The break-point between the integrated photometry and star counts occurs at a radial distance of ~ 88′ (20 kpc). Grey diamonds (86′ < R < 90′) are significantly contaminated by the background and have no reliable uncertainties.

In each bin, number densities were converted to surface brightness [mag arcsec^{-2}] by the following relation: $\mu = \mu_\circ - 2.5 \log (NA^{-1})$, where N is the sum of robust number counts, given by $P(M31)\times(\text{Completeness})^{-1}$, and A is the enclosed area in [arcsec^2]. Since number counts do not have an absolute calibration value, we adjusted $\mu_\circ$ to fix the first bin at $\mu = 26$. The Poisson noise model was used for estimating the uncertainties associated with random counts. Including the contribution due to the ignored objects, the absolute difference for extreme cases was added to the Poisson noise in quadrature. We measured surface brightness profiles at both 3.6 and 4.5 μm and found the two profiles to be quite similar as also noted by Courteau et al. (2011).

Table 5 gives the combined surface brightness profile from both integrated photometry and star counts. Fig. 9 shows the star count profile that has been shifted to illustrate the continuation of the integrated light. Shifting the star count profile to match the integrated light profile results in a change in profile slope at the matching point. We suspect that this reflects the difficulty in determining the appropriate background levels for the two profiles rather than a true physical change in profile slope. The availability of point-source photometry with higher spatial resolution (and thus less affected by crowding) in the overlap region would help to overcome this difficulty. This should be possible with future facilities such as the *James Webb Space Telescope*.

Table 5. IRAC M31 surface brightness profile. This table serves as a guide for the full table, available in its entirety in a machine-readable form in the online journal. () enclose values with no reliable uncertainties.

R_{deproj} (arcmin)	median surface brightness (3.6 μm mag arcsec^{-2})	source
0.02625	11.245 ± 0.260	integrated
0.10526	12.244 ± 0.037	integrated
0.23757	12.838 ± 0.028	integrated
...	...	...
64.7646	20.775 ± 0.234	integrated
67.8535	(21.079 ± 0.000)	integrated
...	...	...
84.5656	(24.909 ± 0.000)	integrated
90.4113	26.000 ± 0.048	star count
105.411	26.423 ± 0.058	star count
...	...	...
195.411	27.362 ± 0.151	star count

6 DISCUSSION AND SUMMARY

We have presented the first results from an extended survey of M31 with *Spitzer*-IRAC at 3.6 and 4.5 μm. We have produced background-corrected mosaics covering total lengths of 4.°4 and 6.°6 along the minor and major axes, respectively. A 3.6 μm-selected catalogue of point sources is presented for 426,529 objects, many of which are detected for the first time. Using auxiliary catalogues we have carried out a statistical analysis in colour-magnitude space to discriminate M31 objects from foreground Milky Way stars and background galaxies. These mosaics and catalogue contain a

wealth of information for Galactic as well as extragalactic studies and they are available for other investigators to use.

One of the original goals of this work was to produce surface brightness profiles by combining the integrated light from background-corrected maps with statistically-treated star counts. Despite the extended coverage of the IRAC mosaics, it is challenging to trace the integrated light for $R > 86'$; the background noise approaches the signal, resulting in very large uncertainty values for the measured flux. In the case of star counts, we face a similar effect due to the foreground and background contaminants – Milky Way dwarfs and star-forming background galaxies are mixed with potential M31 objects in the mid-infrared CMD. As a result, bins beyond $R \sim 200'$ exhibit no robust fall-off or feature (within the uncertainty range). In the inner regions ($R < 90'$), star counts suffer from significant crowding and are thus unreliable due to incompleteness. Because of the difference in sources of contaminants and hence the difference in methods for overcoming these effects in the two profiles, background levels are prone to inconsistency. Therefore, we refrained from extrapolating and/or normalising profiles in the overlapping region at $R \sim 88'$. We conclude that modelling the combined bulge, disc, and halo of the galaxy over a wide range of radii will require combining the IRAC M31 surface brightness profile with other multiwavelength data. Our integrated light profile is *not* based on any isophotal fitting algorithm, and should thus be reproducible and easily comparable to future studies.

In addition to further work on the galaxy structure, a number of future studies are possible with the extended M31 dataset. Examples include stellar population studies via comparison with visible-light datasets such as PAndAS (McConnachie et al. 2009) and PHAT (Dalcanton et al. 2012), searches for dusty extreme-asymptotic-giant-branch stars as in Boyer et al. (2015), comparing a larger sample of M31 globular clusters' mid-infrared colours to population synthesis models as in Barmby & Jalilian (2012), and determining the mid-infrared properties of a uniquely-selected population of quasars in the M31-background (Huo et al. 2015). Data-mining of the catalogue for unusual objects which could be followed-up with higher-resolution infrared imaging or spectroscopy is another possible direction, as is exploration of stellar variability. The Andromeda galaxy provides us with a diversity of physical conditions and star formation histories to explore, with mid-infrared imaging comprising an important spectral region to fully understand our neighbouring galaxy's story.

ACKNOWLEDGEMENTS

MRR thanks Sahar Rahmani for technical support. We thank Steven Willner for providing fruitful comments on the initial manuscript; Stéphane Courteau for providing surface brightness profiles from Courteau et al. (2011); Alan W. McConnachie and the entire PAndAS collaboration for providing access to the PAndAS catalogue. This work is based on observations made with the *Spitzer Space Telescope* and has made use of the NASA/IPAC Infrared Science Archive, both operated by the Jet Propulsion Laboratory, California Institute of Technology, under contract with the National Aeronautics and Space Administration. Support for this work was provided by NASA and by a Discovery Grant from the Natural Science and Engineering Research Council, Canada. This research made use of NASA's Astrophysics Data System; MONTAGE, funded by the National Science Foundation under Grant Number ACI-1440620, and was previously funded by the National Aeronautics and Space Administration's Earth Science Technology Office, Computation Technologies Project, under Cooperative Agreement Number NCC5-626 between NASA and the California Institute of Technology; TOPCAT, an interactive graphical viewer and editor for tabular data (Taylor 2005); the facilities of the Canadian Astronomy Data Centre operated by the National Research Council of Canada with the support of the Canadian Space Agency; and Digitized Sky Survey, retrieved via Aladin (Bonnarel et al. 2000). The Digitized Sky Surveys were produced at the Space Telescope Science Institute under U.S. Government grant NAG W-2166. The images of these surveys are based on photographic data obtained using the Oschin Schmidt Telescope on Palomar Mountain and the UK Schmidt Telescope. The plates were processed into the present compressed digital form with the permission of these institutions.

Facilities: Spitzer Space Telescope (IRAC)

REFERENCES

Arendt R. G., Kashlinsky A., Moseley S. H., Mather J., 2010, ApJS, 186, 10
Aringer B., Girardi L., Nowotny W., Marigo P., Lederer M. T., 2009, A&A, 503, 913
Ashby M. L. N., et al., 2009, ApJ, 701, 428
Athanassoula E., Beaton R. L., 2006, MNRAS, 370, 1499
Bagheri G., Cioni M.-R. L., Napiwotzki R., 2013, A&A, 551, A78
Barmby P., Jalilian F. F., 2012, AJ, 143, 87
Barmby P., et al., 2006, ApJ, 650, L45
Barmby P., Huang J.-S., Ashby M. L. N., Eisenhardt P. R. M., Fazio G. G., Willner S. P., Wright E. L., 2008, ApJS, 177, 431
Beaton R. L., et al., 2007, ApJ, 658, L91
Bertin E., Arnouts S., 1996, A&AS, 117, 393
Bianchi L., 2009, Ap&SS, 320, 11
Bonnarel F., et al., 2000, A&AS, 143, 33
Boyer M. L., Skillman E. D., van Loon J. T., Gehrz R. D., Woodward C. E., 2009, ApJ, 697, 1993
Boyer M. L., et al., 2015, ApJS, 216, 10
Chen Y., Girardi L., Bressan A., Marigo P., Barbieri M., Kong X., 2014, MNRAS, 444, 2525
Corbelli E., Lorenzoni S., Walterbos R., Braun R., Thilker D., 2010, A&A, 511, A89
Courteau S., Widrow L. M., McDonald M., Guhathakurta P., Gilbert K. M., Zhu Y., Beaton R. L., Majewski S. R., 2011, ApJ, 739, 20
Dalcanton J. J., et al., 2012, ApJS, 200, 18
Fazio G. G., et al., 2004, ApJS, 154, 39
Fingerhut R. L., et al., 2010, ApJ, 716, 792
Geehan J. J., Fardal M. A., Babul A., Guhathakurta P., 2006, MNRAS, 366, 996
Girardi L., Groenewegen M. A. T., Hatziminaoglou E., da Costa L., 2005, A&A, 436, 895
Girardi L., et al., 2010, ApJ, 724, 1030
Gordon K. D., et al., 2006, ApJ, 638, L87
Groenewegen M. A. T., 2006, A&A, 448, 181
Guhathakurta P., Ostheimer J. C., Gilbert K. M., Rich R. M., Majewski S. R., Kalirai J. S., Reitzel D. B., Patterson R. J., 2006, preprint, (arXiv:astro-ph/0502366v5)
Huo Z.-Y., et al., 2015, Res. Astron. Astrophys., 15, 1438
Ibata R., Martin N. F., Irwin M., Chapman S., Ferguson A. M. N., Lewis G. F., McConnachie A. W., 2007, ApJ, 671, 1591
Ibata R. A., et al., 2014, ApJ, 780, 128
Irwin M. J., Ferguson A. M. N., Ibata R. A., Lewis G. F., Tanvir N. R., 2005, ApJ, 628, L105
Jacob J. C., et al., 2009, Int. J. Comput. Sci. Eng., 4, 73
Jarrett T. H., et al., 2011, ApJ, 735, 112

Krick J. E., Glaccum W. J., Carey S. J., Lowrance P. J., Surace J. A., Ingalls J. G., Hora J. L., Reach W. T., 2012, ApJ, 754, 53
Makovoz D., Khan I., Masci F., 2006, Proc. SPIE, 6065, 330
Marigo P., Girardi L., Bressan A., Groenewegen M. A. T., Silva L., Granato G. L., 2008, A&A, 482, 883
McConnachie A. W., Irwin M. J., Ferguson A. M. N., Ibata R. A., Lewis G. F., Tanvir N., 2005, MNRAS, 356, 979
McConnachie A. W., et al., 2009, Nature, 461, 66
McQuinn K. B. W., et al., 2007, ApJ, 664, 850
Reach W. T., et al., 2005, PASP, 117, 978
Rix H.-W., Rieke M. J., 1993, ApJ, 418, 123
Schuster M. T., Marengo M., Patten B. M., 2006, Proc. SPIE, 6270, 627020
Sheth K., et al., 2010, PASP, 122, 1397
Skrutskie M. F., et al., 2006, AJ, 131, 1163
Spitzer Science Center 2015, Spitzer-IRAC Instrument Handbook, v2.1.2 edn. SSC, Pasadena, CA
Tanaka M., Chiba M., Komiyama Y., Guhathakurta P., Kalirai J. S., Iye M., 2010, ApJ, 708, 1168
Taylor M. B., 2005, ASP Conf. Ser., 347, 29
Thilker D. A., et al., 2007, ApJS, 173, 538
Wright E. L., et al., 2010, AJ, 140, 1868
de Vaucouleurs G., de Vaucouleurs A., Corwin Jr. H. G., Buta R. J., Paturel G., Fouqué P., 1991, Third Reference Catalogue of Bright Galaxies. Volume II: Data for galaxies between 0^h and 12^h.. Springer, New York, NY

This paper has been typeset from a TEX/LATEX file prepared by the author.